CONDENSED MATTER PHYSICS

An in-plane photoelectric effect in two-dimensional electron systems for terahertz detection

Wladislaw Michailow[1]*, Peter Spencer[1], Nikita W. Almond[1], Stephen J. Kindness[1], Robert Wallis[1], Thomas A. Mitchell[1], Riccardo Degl'Innocenti[2], Sergey A. Mikhailov[3], Harvey E. Beere[1], David A. Ritchie[1,4]

Copyright © 2022 The Authors, some rights reserved; exclusive licensee American Association for the Advancement of Science. No claim to original U.S. Government Works. Distributed under a Creative Commons Attribution License 4.0 (CC BY).

Many mid- and far-infrared semiconductor photodetectors rely on a photonic response, when the photon energy is large enough to excite and extract electrons due to optical transitions. Toward the terahertz range with photon energies of a few milli–electron volts, classical mechanisms are used instead. This is the case in two-dimensional electron systems, where terahertz detection is dominated by plasmonic mixing and by scattering-based thermal phenomena. Here, we report on the observation of a quantum, collision-free phenomenon that yields a giant photoresponse at terahertz frequencies (1.9 THz), more than 10-fold as large as expected from plasmonic mixing. We artificially create an electrically tunable potential step within a degenerate two-dimensional electron gas. When exposed to terahertz radiation, electrons absorb photons and generate a large photocurrent under zero source-drain bias. The observed phenomenon, which we call the "in-plane photoelectric effect," provides an opportunity for efficient direct detection across the entire terahertz range.

INTRODUCTION

Transforming light to electricity belongs to the range of problems that have both a deep fundamental importance and a great impact on modern technology. The influence of light on electrical processes has been studied since the late 19th century and led to the discovery of the photoelectric effect. In 1902, Lenard found that the energy of electrons emitted from a metal under irradiation by x-rays depends only on the frequency, but not the intensity, of the incident light (*1*). This puzzling observation stimulated Einstein in 1905 to put forward the idea that formed the foundation to the development of quantum mechanics: Light is absorbed in the form of discrete quanta (photons), and a photon can excite an electron from the surface of a metal, if its quantized energy $\hbar\omega$ is larger than the potential step height formed at the material interface—the work function (*2*). The photoelectric effect provides a way of detecting electromagnetic radiation by measuring the light-generated current or voltage or by registering changes of the electrical conductivity of a material under irradiation.

The work function of most solid-state materials lies in the range of several electron volts; therefore, the conventional, external photoelectric effect with electron emission from a material into vacuum can only be used for detection of ultraviolet and higher energy radiation. At lower frequencies, near infrared to visible, the photovoltaic effect can be used for conversion of light to electricity, e.g., in solar cells, via interband excitation of electrons across the bandgap between the valence and conduction bands. At even lower frequencies, mid to far infrared, this process becomes inaccessible because of the lack of semiconductors with suitably low bandgaps, and researchers exploit instead intraband transitions in semiconductors in the internal photoelectric effect. This can be electron photoexcitation from a confined ground state into a higher-energy quantum state, as in the case of, e.g., quantum well infrared photodetectors (QWIPs) (*3*, *4*) and quantum dot infrared photodetectors (*5*), stressed Ge:Ga blocked impurity band detectors (BIBs) (*6*, *7*), or continuum-to-continuum photoexcitation in heterojunction or homojunction internal photoemissive detectors (HEIWIP and HIWIP) (*8*–*11*). Another detector type based on intersubband transitions are tunable antenna-coupled intersubband terahertz (TACIT) detectors (*12*–*14*), which rely not on electron extraction but on the bolometric heating and change in conductance as a result of electrons in a quantum well being promoted into an excited subband.

Several properties are inherent to detectors relying on charge carrier extraction via the internal photoelectric effect (*15*). These detectors have a lower frequency limit, which, in practice, results in a rapid falloff of their responsivity toward the terahertz (THz) range. The frequency threshold is given, for example, by the doping or material-dependent potential step at the boundary of, e.g., n^+ and i areas in the internal photoemissive detectors. In GaAs/$Al_xGa_{1-x}As$ heterostructure-based detectors such as HEIWIPs, the frequency threshold tunability is limited by the practically achievable alloy ratio of $x = 0.005$; in HIWIPs, the lower frequency is restricted by the achievable emitter doping concentration (*15*, *16*). In BIBs, the lower frequency limit depends on the ionization energy of donor states. In addition, readout or the extraction of electrons is usually done in photoconductive mode, under the presence of an external bias (*6*, *7*, *17*–*19*), which represents an additional noise source.

A more general, crucial issue of detectors relying on optical transitions (including intraband and intersubband) results from the transverse nature of the electromagnetic waves. The natural way of detecting electromagnetic radiation would be to send the light normally onto the material surface. In this case, the electric field vector is parallel to the material interface and couples to the electron momentum parallel to the interface (*20*). However, to contribute to the photocurrent, electrons need to obtain sufficient momentum perpendicular to the material interface to overcome the potential barrier (in the internal photoemissive detectors) or to jump into the first excited subband (in the quantum well intersubband detectors) (*3*, *19*). Electrons may obtain the necessary momentum using oblique or grazing incidence of p-polarized light (*21*–*23*) or through scattering

[1]Cavendish Laboratory, University of Cambridge, JJ Thomson Avenue, Cambridge CB3 0HE, UK. [2]Department of Engineering, University of Lancaster, Bailrigg, Lancaster LA1 4YW, UK. [3]Institute of Physics, University of Augsburg, 86135 Augsburg, Germany. [4]Swansea University, Singleton Park, Sketty, Swansea SA2 8PP, UK.
*Corresponding author. Email: wm297@cam.ac.uk

Downloaded from https://www.science.org at Universitaetsbibliothek Augsburg on May 23, 2022

processes (*24*). Both cases are not optimal, and scattering reduces the efficiency of the process and limits the response time to the scattering times. To mitigate against this problem, more complicated designs are necessary to increase the light-matter coupling to obtain an electric field component perpendicular to the interface (*3*), e.g., by using a grating (*4*) or by placing two wings of a THz antenna below and above the active detector layers in TACIT detectors (*13*).

To date, at the low-frequency end of the THz range, Schottky diodes provide highly sensitive room temperature detection with commercially available bandwidths of 40 GHz (*25*), but they suffer from rapidly decreasing responsivity $\sim 1/\omega^2$ above 1 THz, being restricted by the resistive-capacitive time constant (*26*, *27*). Detectors such as QWIPs, HIWIPs, and HEIWIPs show promising higher-frequency performance, but practical demonstrations show a rapid decrease toward the range of 2.5 to 3 THz from above (*16*, *18*, *28*). While highly sensitive THz detectors are available in the range of 1 to 3 THz, e.g., stressed Ge:Ga detectors (*6*, *7*) or high-speed superconducting hot electron bolometers (*29*–*31*), they are restricted to operational temperatures around the liquid helium range. Hence, the search for alternative detector schemes in the THz gap is still going on.

Recently emerged detectors based on field-effect transistors provide a good compromise for practical applications (*32*–*40*). They feature a compact design allowing for easy integration in devices using state-of-the-art semiconductor processing technology and can be tailored for high responsivities (*41*–*43*), high bandwidth, and high damage threshold (*44*). The main operation mechanism of these detectors is referred to as plasmonic mixing (*32*, *33*, *45*) or distributed resistive mixing (*41*, *46*). Other mechanisms that give rise to a THz photoresponse in gated two-dimensional electron gases (2DEGs) can be of a thermal nature, such as the photothermoelectric effect (*47*–*49*), the bolometric effect (*50*), and collisionless electron heating (*51*), or are based on photonic processes, such as photon-assisted tunneling (*52*–*55*) or the photovoltaic effect (*56*), the latter being present in materials such as gapless graphene where charge carriers of both signs exist (electrons and holes).

In this work, we present a new quantum, photonic mechanism of THz photoresponse generation in 2DEGs, which exceeds the response expected from plasmonic mixing in our device by more than an order of magnitude and cannot be explained by other known mechanisms mentioned above. In our experiment, we create an artificial, in situ electrically tunable potential step for electrons moving within the 2D channel. This way, we create a material interface within the plane of the 2DEG, between two regions of different electron density controlled by two independently biased gates. Normally incident THz radiation leads then to an electron flow across this step, parallel to the semiconductor surface. On both sides of the potential step, the chemical potential of the 2DEG lies above the conduction band edge, so that the photoresponse is observed under zero source-drain bias. The dual-gated device architecture allows independent tunability of responsivity and output impedance of the device, facilitating in situ impedance matching to external readout electronics.

We will call this phenomenon the in-plane photoelectric effect. In contrast to the conventional 3D photoelectric effect, it has a number of remarkable features and is observed under conditions where the 3D photoelectric effect cannot be observed. We have developed a quantum theory of the in-plane photoelectric effect, which describes the experimental findings very well and shows that the discovered phenomenon is highly promising for efficient photodetection across the entire THz range.

RESULTS

Physics of the in-plane photoelectric effect

Consider a uniform 2DEG covered by two gates (see Fig. 1A). In equilibrium, the bottom of the conduction band (magenta dashed line) and the chemical potential μ are position independent. By applying two different voltages on the gates, $U_{G,L}$ and $U_{G,R}$, we create an artificial, gate voltage tunable potential step for electrons moving in the 2DEG. This shifts the bottom of the equilibrium conduction band under the left and right gates by V_L and V_R, respectively, resulting in the local chemical potentials μ_L and μ_R (see Fig. 1B). Without any incident radiation, the net particle flow vanishes: Electrons with energies $E < V_L$ do not contribute to the current because they are reflected backward at the step, while, for $E > V_L$, the current flow cancels out because of equal reflection and transmission probabilities regardless of the direction of electron motion.

Once the potential step in the gap between the gates is exposed to incident electromagnetic radiation of frequency $f = \omega/(2\pi)$, electrons can absorb a photon of energy $\hbar\omega$. Those with energies $E < V_L$ on the right side, which previously could not overcome the step, are now able to do so by an instantaneous process of photoexcitation. For electrons with energies $V_L < E < \mu$, photon absorption will lead to a higher probability to move to the left (onto the step) than to the right. The probabilities of particles incident from the left ($P^{\rightarrow}$) and from the right ($P^{\leftarrow}$) to absorb a photon and keep moving in the same direction can be calculated (see the "Theory" section), and Fig. 1C illustrates the resulting probabilities for $\hbar\omega = 8$ meV, $V_L = 5$ meV, and $V_R = -5$ meV. Below $V_L - \hbar\omega$, both probabilities $P^{\leftarrow}$ (blue curve) and $P^{\rightarrow}$ (red curve) are zero, because even the absorption of a photon will not help to overcome the potential step. There are no electrons with energies $E < V_L$ on the left of the potential step; hence, $P^{\rightarrow}$ is zero for $E < V_L$. Electrons incident from the right with energies $V_L - \hbar\omega < E < V_L$ have insufficient energy to pass the potential step but are able to overcome it by absorbing an incident photon, which is shown by the finite $P^{\leftarrow}$ in this region. This probability grows from zero at $E = V_L - \hbar\omega$ up to a finite value at $E = V_L$. At $E > V_L$, the probability $P^{\rightarrow}$ starts to grow, while the probability $P^{\leftarrow}$ starts to decrease from its maximum value. For $E \gg V_L$, $P^{\rightarrow}$ and $P^{\leftarrow}$ tend to the same values, as electrons with very high energies barely notice the presence of the potential step.

It should be noted that, for all energies E, the probability of photoexcited electrons to move onto the potential step—from the higher-density region to the lower-density region—is always higher than in the opposite direction. As a result, the radiation induces a net particle flow from the higher-density region to the lower-density region. We use this in-plane photoelectric effect for THz detection in a 2DEG covered by two gates, which simultaneously serve as a THz antenna.

Samples and setup

Our samples (see Fig. 2A) are fabricated from a GaAs-$Al_{0.33}Ga_{0.67}As$ heterostructure grown by molecular beam epitaxy with a 2DEG $d \approx$ 90 nm below the surface (see details in Materials and Methods). Narrow channels were created by mesa etching. A bow-tie antenna of 17-μm radius (see Fig. 2B) focuses the incident THz radiation on the active part of the device. The two wings of the antenna simultaneously serve as independently biased gates, which can be used to create a potential step in the 2DEG as shown in Fig. 2B (inset). Compared to Fig. 1A, in the real device, the gates have finite widths and are asymmetric. The right antenna wing, the "narrow gate," is split into two halves that are joined together via a 200-nm narrow

Downloaded from https://www.science.org at Universitaetsbibliothek Augsburg on May 23, 2022

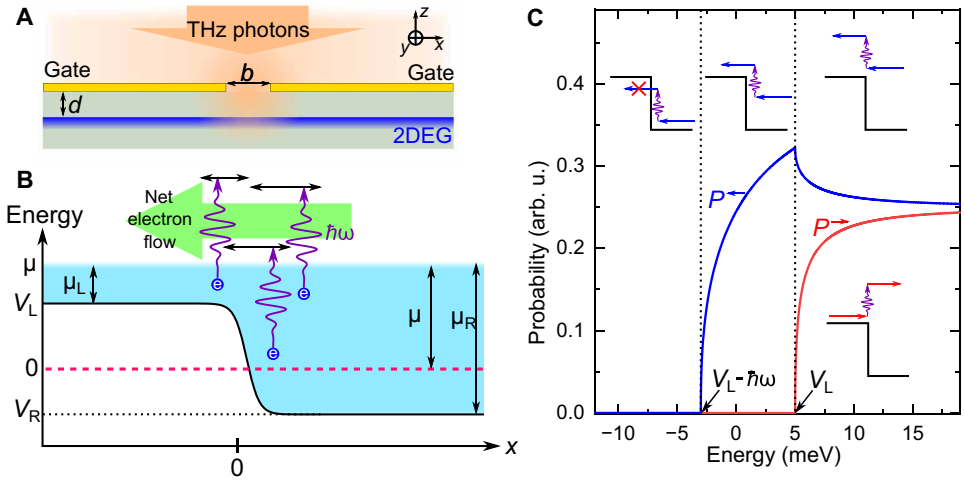

Fig. 1. Physical principle of the in-plane photoelectric effect. (**A**) Side view of the device: A semiconductor heterostructure with a 2D electron gas is covered by two gates and irradiated by electromagnetic radiation. (**B**) Energy diagram of the device. μ is the equilibrium chemical potential, and $V_L > 0$ and $V_R < 0$ are the conduction band edges in the left and right parts of the device. A potential step of value $V_L - V_R$ is artificially created by applying different voltages to the gates. This gives rise to different electron densities and different chemical potentials, $\mu_L = \mu - V_L$ and $\mu_R = \mu - V_R$, in the left and right areas of the 2D electron gas. Incident electromagnetic radiation on a potential step excites electrons on both sides of the barrier, resulting in a net electron flow onto the step. (**C**) Energy dependence of the probability to absorb a photon and pass the step for electrons moving from right to left (blue curve) and from left to right (red curve) (see Materials and Methods). The curves are plotted for $\hbar\omega = 8$ meV, $V_L = 5$ meV, and $V_R = -5$ meV. The insets illustrate the physical processes described by the blue and red curves in the respective energy intervals. (arb. u. = arbitrary units.).

bridge (Fig. 2B). The left "wide gate" has no cutout, and electrons underneath it have to pass a distance of $\gtrsim$4 μm from the narrow channel to escape into the ungated source 2DEG connections. The 2DEG has four ohmic contacts, labeled source 1 or 2 and drain 1 or 2, which are at least 100 μm away from the center of the antenna to avoid their influence on the active part of the device (see fig. S1). THz detection is then carried out by a two-terminal photocurrent or photovoltage measurement for which one source and one drain contact are sufficient; all four contacts are used only for four-terminal conductance measurements.

The devices were cooled to 9 K ($k_BT \approx 0.78$ meV) in a liquid-helium continuous-flow cryostat. A copper waveguide system delivered 1.9-THz ($\hbar\omega \approx 7.9$ meV) radiation from a THz quantum cascade laser (QCL) source (*57*) to the samples. The QCL is electrically modulated with a modulation frequency of $f_{mod} = 781$ Hz and a duty cycle of 2.14%. The time-averaged intensity at the position of the sample (without considering interference effects in the waveguided THz system) is $\langle I \rangle \approx 6.3\ \mu W/mm^2$ and is used for subsequent estimations; for details, see Materials and Methods. This value corresponds to an intensity during the pulse of $\langle I \rangle/(2.14\ \%) \approx 0.29\ mW/mm^2$. We observed similar THz responses, both qualitatively and quantitatively, on three THz detectors of identical fabrication geometry and present results on a representative sample.

Photoresponse and device parameters

Figure 3A illustrates the conductance of the sample, measured in a four-terminal configuration, as a function of the two gate voltages in a 2D colormap. At zero gate voltages, the four-wire channel resistance is $R_0 \approx 1.1$ kilohm. The conductance vanishes at the left and at the bottom of the map, which corresponds to the pinch-off of the channel using the wide or narrow gate, respectively. The threshold voltage is $U_{th} \approx -0.43$ V, and the equilibrium electron density at zero gate voltage is $n_0 = 2.9 \times 10^{11}/cm^2$ (see Supplementary Text and fig. S4). This corresponds to an equilibrium chemical potential of $\mu = \pi\hbar^2 n_0/m_{eff} \approx$ 12 meV, with the effective electron mass $m_{eff} = 0.067 m_e$ in GaAs (*58*).

Under incident THz radiation, the sample generates a photoresponse. The induced current under zero source-drain bias, the photocurrent, is measured using a current preamplifier and is shown in Fig. 3B. Similarly, the THz photovoltage is depicted in Fig. 3C. The measurements are carried out using a lock-in amplifier with the QCL modulation frequency f_{mod} as reference. The red and blue color schemes indicate areas where the response is positive or negative, respectively.

The photoresponse arises predominantly in the left or bottom areas in the 2D maps Fig. 3 (B and C), where either of the narrow- or wide-gate voltages are negative. Here, one of the gates depletes the 2DEG, which gives rise to a potential step in the channel. The sign of the photoresponse is always such that the THz-induced electron flow moves onto the potential step, from the higher-density region to the lower-density region. The photoresponse is mostly antisymmetric with respect to the diagonal line $U_{G,narrow} = U_{G,wide}$. Two regimes can be identified: (i) $U_{G,wide}$ and $U_{G,narrow} \lesssim 0.6$ V, shown in detail in Fig. 3E, and (ii) $U_{G,wide}$ or $U_{G,narrow} \gtrsim 0.6$ V, where the photoresponse increases strongly in the top-left and bottom-right corners under strong asymmetry of the chemical potentials.

A further increase of the gate voltage, beyond $U_{G,narrow} > 0.885$V and $U_{G,wide} > 0.75$V, leads to the onset of a rapidly growing gate leakage. In this regime, undesirable for detector operation, the sample becomes unstable and noisy. Blocking and unblocking the incident THz radiation did not result in any change (within measurement accuracy of 10 pA) of the gate currents. This excludes gate currents as a possible origin of the photoresponse, e.g., due to Schottky barrier rectification.

A negative voltage on the narrow gate creates a barrier of 0.2-μm width, whereas, on the wide gate, it creates a $\gtrsim$4-μm-wide barrier (Fig. 2B). A remarkable result is that the photoresponse changes by less than 30% (Fig. 3, B and C, top left versus bottom right), despite

Downloaded from https://www.science.org at Universitaetsbibliothek Augsburg on May 23, 2022

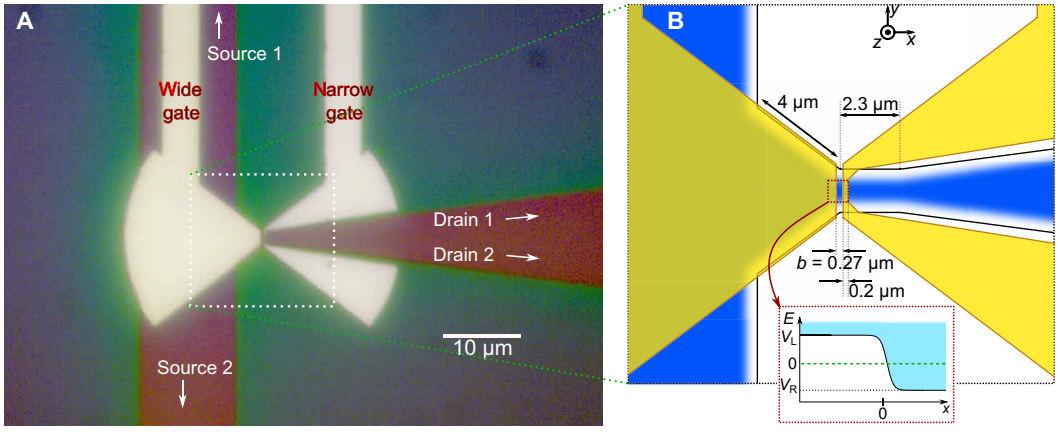

Fig. 2. Sample view. (**A**) Optical microscope image of the sample: The wide and narrow gates are made in the form of a bow-tie antenna; the 2DEG is contacted by two source and two drain ohmic contacts. (**B**) Schematic illustration of the device: The black contour shows the outline of the mesa, while the blue area shows the 2DEG. Its blurred edges account for uncertainty in the amount of edge depletion; $W \sim 0.5$ to 1 μm. The metallized gates are shown semitransparent in yellow. The red box shows the region of interest where the THz radiation is focused. The inset shows the corresponding band diagram along the length of the channel under differently biased gate wings of the antenna.

a more than 20-fold difference in barrier width. This rules out a tunneling origin of the effect.

The best photovoltage performance is achieved at the point ($U_{G,wide}$, $U_{G,narrow}$) = (−0.45 V, 0.885 V) (Fig. 3C), where the resistance is ~70 kilohm. At this point, Fig. 4A shows the source-drain voltage measured using a dc voltmeter, while the THz radiation is mechanically blocked and unblocked. The observation of a clear dc response demonstrates that the device can operate as a direct THz detector. The measured dc photovoltage at the incident time-averaged intensity $\langle I \rangle \approx 6.3\ \mu W/mm^2$ is 56 μV.

Optimal photocurrent readout is achieved at the point ($U_{G,wide}$, $U_{G,narrow}$) = (−0.32 V, 0.885 V) in Fig. 3B, where the low-output impedance of the device, ~2.6 kilohm, allows for fast detection of the photocurrent. Notably, the best photocurrent is thus achieved when the device is far from pinch-off: The channel resistance is merely 2.4 times higher than at zero gate voltages. Figure 4B shows the response to incident THz pulses from the QCL on a microsecond time scale under these conditions. During a pulse, the THz intensity $I_0 \approx 0.29\ mW/mm^2$ at the detector position yields a photocurrent of ~142 nA.

The physical dimensions of the active part of the THz detector device, i.e., the bow-tie antenna, are much smaller than the free-space wavelength of the THz radiation. To evaluate the detector's internal responsivity, we choose to use the absorption cross section of the device as the most appropriate normalization area, which we calculated to be $(22.5\ \mu m)^2 \approx 506\ \mu m^2$ using numerical finite-element simulations in COMSOL Multiphysics (see Supplementary Text). Using this normalization area, the above values of the photoresponse give an estimate for the internal responsivity of the device, normalized to the absorbed power and without considering possible interference effects (see Materials and Methods), of 17 kV/W (photovoltage) and 0.96 A/W (photocurrent), respectively.

A key advantage of the two gates is the independent tuning of output impedance and responsivity. This enables impedance matching to external circuitry—a capability that is inherently built-in into the device design. The target working point for a desired photocurrent response and output impedance, i.e., the two gate voltages, is to be determined from the intersection of equi-photocurrent contours in Fig. 3B with equi-conductance contours in Fig. 3A. This also means that detection sensitivity can be switched on or off with the gate voltages while maintaining the device's impedance, thus making it appear the same in the external circuit. The available responsivity and output impedance ranges can be found in fig. S5.

Theory

We consider a narrow 2DEG under two semi-infinite gates. The gate voltages $U_{G,L}$ and $U_{G,R}$ induce a smooth-step potential $V_0(x)$ (Fig. 1B). Under THz irradiation, an additional localized ac electric field appears in the gap region between the gates and gives rise to an additional time-dependent potential $V_1(x, t)$. To get an analytical solution of the problem, we model these potentials as $V_0(x) = V_L - (V_L - V_R)\Theta(x)$ and $V_1(x, t) = \Delta\phi_{ac}(\mathrm{sign}(x)/2)\cos(\omega t)$, where $\Theta(x)$ is the Heaviside step function. $\Delta\phi_{ac} \approx E_{ac} b$ is the potential difference induced by the ac electric field acting on the 2DEG at the step in the x direction with amplitude E_{ac}. Because the mean free path in the 2DEG $\lambda_e \gtrsim 11$ μm is much larger than $b = 0.27$ μm, electrons are assumed to pass the gap between the antenna wings ballistically. In the y direction, an infinite potential well of width W is assumed ($W \approx 0.7$ μm), so that the ground-state energy of the transverse motion is $E_W = \pi^2\hbar^2/(2m_{eff}W^2) \approx 12$ μeV; for details, see Materials and Methods.

To describe the photoresponse of the system, we solve the time-dependent Schrödinger equation in the first-order perturbation theory, treating V_1 as a perturbation (see Materials and Methods). The resulting expression for the photocurrent is

$$I_{ph} = ef\left(\frac{eE_{ac}b}{\hbar\omega}\right)^2\left[2\sqrt{\frac{\hbar\omega}{E_W}}J\left(\frac{\mu_L}{\hbar\omega}, \frac{\mu_R}{\hbar\omega}\right)\right] \quad (1)$$

The photocurrent's dependence on the chemical potentials is described by a universal dimensionless function J that depends on the two dimensionless parameters $\mu_L/(\hbar\omega)$ and $\mu_R/(\hbar\omega)$ and is antisymmetric (see Fig. 3D). The gates are pinched off at $\mu_{L/R} = 0$. In the area with $\mu_L < 0$ and $\mu_R < 0$, where there are no electrons in both parts of the sample, the photocurrent vanishes. When only one of the chemical potentials is negative, down to $-\hbar\omega$, the function J is nonzero: Photoexcited electrons are still able to jump onto the step

Downloaded from https://www.science.org at Universitaetsbibliothek Augsburg on May 23, 2022

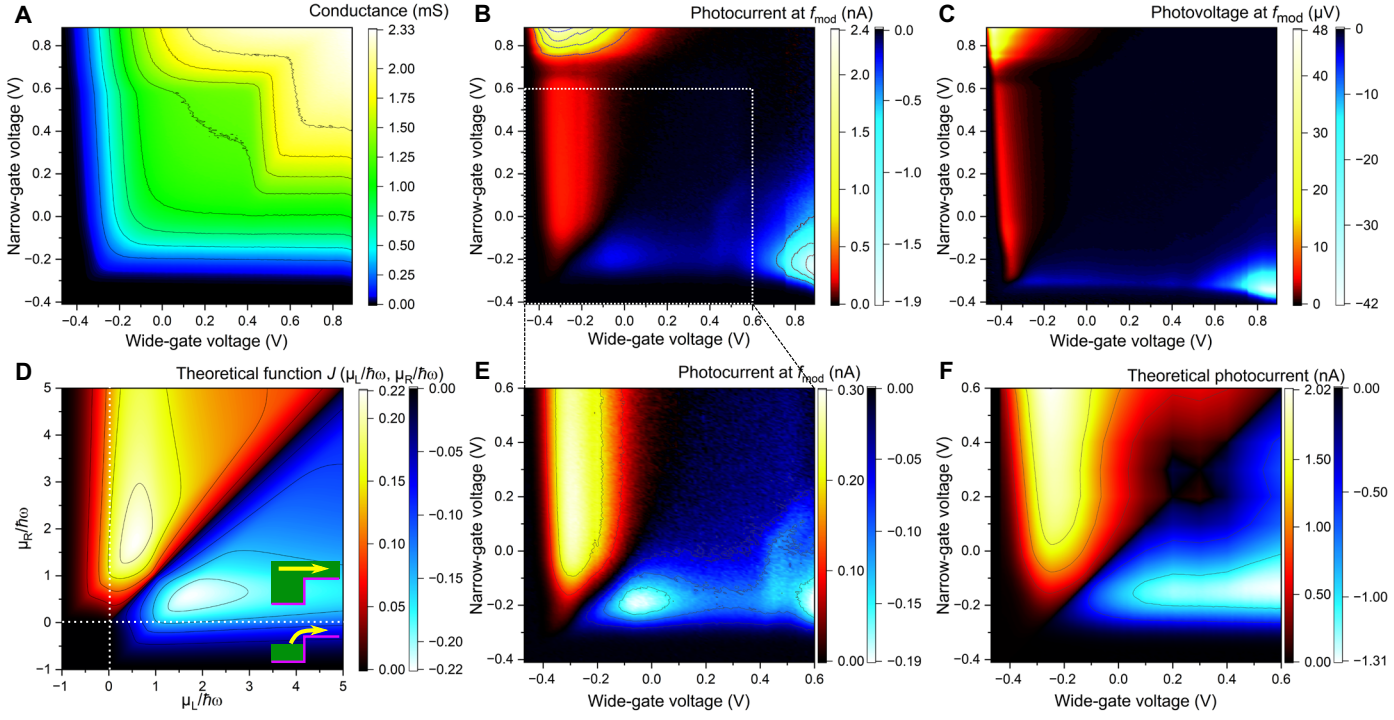

Fig. 3. Gate-voltage–dependent measured device parameters and supporting theoretical calculations. Experimental results: (**A** to **C** and **E**) 2D maps as a function of wide-gate voltage (horizontal axis) and narrow-gate voltage (vertical axis): (A) four-wire conductance of the device; (B) photocurrent, with a detailed plot of the region $U_{G,wide}$, $U_{G,narrow}$ < 0.6V in (E); (C) photovoltage. The photoresponse to incident THz radiation is measured as time-averaged value at the modulation frequency of the QCL, corresponding to the time-averaged intensity $\langle I \rangle = 6.3\ \mu W/mm^2$. Theoretical calculations: (**D**) Function $J(\mu_L/\hbar\omega; \mu_R/\hbar\omega)$ defined by Eq. 1 with insets showing the respective processes. (**F**) Theoretically expected photocurrent in the region $U_{G,wide}$, $U_{G,narrow}$ < 0.6 V with resistive loading taken into account. Negative and positive values in (B) to (F) are presented in separate color bars. Contour line values are indicated on the color bars.

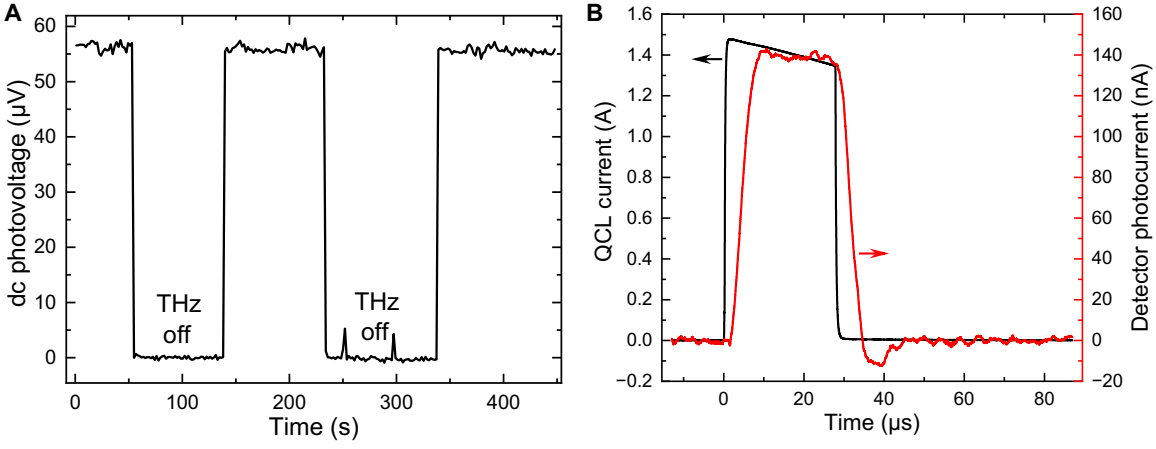

Fig. 4. THz detection with the presented device. (**A**) dc source-drain voltage response in photovoltage readout mode, when the THz waveguide is repeatedly mechanically blocked and unblocked. When the THz waveguide is open, QCL emission with 2.14% duty cycle is incident on the sample. A maximum time-averaged dc photovoltage of 56 μV is induced by the electrically modulated QCL emission. (**B**) Sample response to incident THz pulses. Left axis: QCL current. Right axis: Measured detector current. A photocurrent of ~142 nA is observed during a THz pulse emitted by the QCL.

when $\mu < V_{L/R} < \mu + \hbar\omega$. This is similar to the "conventional" photoelectric effect, with a "work function" corresponding to $-\mu_{L/R} = V_{L/R} - \mu$ (see Fig. 3D, bottom inset). However, this region is of little significance for the experimentally observed photoresponse: In practice, the very large channel resistance beyond the pinch-off strongly suppresses the photocurrent.

The main features of the in-plane photoelectric effect are located at positive chemical potentials. The maximum of the function $J(\mu_L/\hbar\omega; \mu_R/\hbar\omega)$ is equal to 0.221 and is located at $\mu_L = 0.57\hbar\omega$ and $\mu_R = 1.73\hbar\omega$. Notably, this corresponds to the open regime far away from pinch-off, where in both parts of the system, $x > 0$ and $x < 0$, electrons form a degenerate Fermi gas with chemical potentials well

Downloaded from https://www.science.org at Universitaetsbibliothek Augsburg on May 23, 2022

above the conduction band edges, as illustrated in Figs. 1B and 3D (top inset). This is in contrast to the conventional photoelectric effect, where the chemical potential always lies below the barrier height.

The relationship between the radiation frequency and the chemical potentials allows to determine the optimal frequency range of the detection mechanism. Because typical electron concentrations $n_0 = m_{\mathrm{eff}}\mu/(\pi\hbar^2)$ in 2DEGs range from ~10^{10}/cm^2 (*59*) to ~$4 \cdot 10^{12}$/cm^2 (*60*), optimal photodetection can be achieved between 0.15 and 20 THz. Apart from the function J, the photocurrent in Eq. 1 contains a prefactor $\sim\omega^{-1/2}$. Thus, the amplitude of the response scales weakly with frequency, which makes the in-plane photoelectric effect ideally suited for detection of radiation in the entire THz range.

The photocurrent given by Eq. 1 is the internal current generated by the potential step. To compare it with the measured photocurrent, the loading of the quantum mechanical current source with the external classical resistances has to be considered. The bare internal resistance R_{in} of the current source cannot be accessed in the experiment but can be estimated theoretically as the inverse of the conductance of the potential step calculated in zeroth order, without THz irradiation (see Eq. 5 in Materials and Methods). The total circuit resistance R_{total} consists of the four-wire sample resistance, which includes R_{in} and is shown in Fig. 3A, the resistance of the connecting leads and ohmic contacts, measured to be approximately 1.82 kilohm, as well as the input impedance of the current amplifier of 100 ohm. The expected photocurrent with external loading is given by $I_{\mathrm{ph,loaded}} = R_{\mathrm{in}} I_{\mathrm{ph}}/R_{\mathrm{total}}$.

In addition, the dependencies on chemical potentials in Eq. 1 and Fig. 3D have to be transformed into gate voltage dependencies. This is done by first translating the chemical potentials μ to the electron density n_s via

$$\mu(U_G) = \pi\hbar^2 n_s(U_G)/m_{\mathrm{eff}} \quad (2)$$

Then, the relationship between electron density n_s and gate voltage U_G was obtained by measuring the electron density from Shubnikov–de Haas oscillations and the Hall effect on a gated Hall bar, made from the same wafer. This way, we get the theoretical photocurrent expected under the experimental conditions, as shown in Fig. 3F.

DISCUSSION

There is a good qualitative agreement with the experimental photocurrent for $U_{\mathrm{G,wide}}$, $U_{\mathrm{G,narrow}} < 0.6$ V in Fig. 3E. The theory predicts photocurrent in the same regions where it is observed experimentally, with the same sign and of the same order of magnitude. The match between theory and experiment is best when considering the red regions with $I_{\mathrm{ph}} > 0$. This is sensible because it corresponds to a barrier under the wide gate, which is a better approximation of a semi-infinite potential step as considered in the theory, than the 200-nm narrow gate. The darker area at positive gate voltages originates from a flat trend of the electron density as a function of the gate voltage in the region of about 0.2 to 0.4 V (see Supplementary Text and fig. S4). Despite the simplicity of the model, all key features are thus reproduced.

The strong increase in photocurrent under maximum asymmetry in the top-left and bottom-right regions in Fig. 3B, at voltages above 0.6 V on one gate, is not covered in the theoretical framework. Qualitatively, it is likely related to the conducting channel becoming wider, as edge depletion effects start to diminish at strongly positive gate voltages. An increase in channel width, which is ~0.5 to 1 μm in equilibrium as indicated in Fig. 2B, would give rise to an increased conductance in Fig. 3A, as the bottleneck in the form of the narrow channel is widened, and also to an enhanced photocurrent $I_{\mathrm{ph}} \sim W$, which increases with the channel width. The quantitative explanation of this effect requires further research.

Quantitatively, the theoretical photocurrent is expected to be up to 1.5 to 2 nA (Fig. 3F). The experimentally measured maximum value in the region $U_{\mathrm{G,wide}}$, $U_{\mathrm{G,narrow}} < 0.6$ V is 0.3 nA (Fig. 3E). The difference may be due to the smoothness of the potential step neglected in the theory and device-related effects such as mobility reduction in the pinch-off area. This indicates that the experimentally observed signal could be further increased by optimizing the wafer structure and device geometry.

It is remarkable that, while the in-plane photoelectric effect gives a value higher than the measured one, other possible interpretations, such as plasmonic mixing (*33*, *45*, *46*), bolometric (*50*), electron heating (*51*), and photothermoelectric effects (*47*, *48*) or photon-assisted tunneling (*54*, *55*), cannot explain the effect or predict a lower value than measured, as we will show in the following.

Bolometric mechanisms commonly give rise to photoconductance, rather than a zero-bias photocurrent or photovoltage (*50*, *51*, *61*), and dominate in the pinch-off regime, where conduction is sensitive to small temperature changes (*50*). In contrast, in our case, the photocurrent is maximal in the open regime. In the case of a broken symmetry, a photocurrent may be observed, e.g., as a (photo)thermoelectric effect (*47*). However, the prerequisite for the applicability of such interpretations is local electron thermalization. However, in our case, the mean free path λ_e of electrons is very large: >11 μm in the wafer material, and even considering a reduction of λ_e within the channel due to the edge roughness, it still exceeds $b = 0.27$ μm, the distance between the gates, which is the relevant length scale. Thus, electrons pass the region between the gates ballistically. This rules out local electron thermalization and mechanisms relying on it.

On the other hand, electron "heating" can also occur in a collisionless way, in the sense that the incident radiation increases the mean electron energy, as in (*51*). The increase in the mean energy of the electrons can be estimated as $e^2 E_{\mathrm{ac}}^2/(4 m_{\mathrm{eff}}\omega^2) \approx 0.46\,\mu\mathrm{eV} \ll k_B T \ll \mu$, which is a negligible amount (for the maximum electric field in the x direction of $E_{\mathrm{ac}} = 100$ V/cm during a THz pulse with intensity I_0, extracted from numerical simulations of the antenna amplification).

Another mechanism to consider is photon-assisted tunneling (*53*–*55*): Photons incident on a thin barrier in the tunneling regime can give rise to photoconductance. However, in the present experiment, the size of the barriers created by the gates is macroscopically large (~4 μm in the case of the wide gate), and the photocurrent dominates in the open regime. This rules out tunneling-related effects such as photon-assisted tunneling.

Many THz detection experiments (*32*–*36*, *38*–*41*, *46*, *62*) were interpreted in terms of the plasma-wave mixing theory (*45*), a mechanism that, at lower frequencies, corresponds to distributed resistive mixing or resistive self-mixing (*41*, *46*). Let us estimate the absolute value predicted by the plasmonic mixing mechanism. In our experiment, the THz gate-to-channel voltage amplitude U_{ac} is equal to 0.18 mV for the average incident power according to numerical antenna simulations. The sample can be modeled as a back-to-back series connection of two 2DEGs with different densities. The source-drain distance is much longer than the plasmon decay length, and $\omega\tau \gg 1$. Under these conditions, the plasmonic

Downloaded from https://www.science.org at Universitaetsbibliothek Augsburg on May 23, 2022

mixing theory (*45*) predicts a photovoltage of 0.2 μV at the point of maximum experimental photocurrent in the $U_G < 0.6$V area, ($U_{G,wide}$, $U_{G,narrow}$) = (−0.29 V, 0.15 V), where the measured photovoltage is 1.8 μV, i.e., considerably higher. Furthermore, the maximum possible photovoltage for nonresonant detection is $\approx e U_{ac}^2/(4\eta k_B T) \sim 1$ μV, according to (*33*), with $\eta \gtrsim 10$ in GaAs-based field-effect transistors at low temperatures (*33*). This is smaller than the experimental photovoltage of 5.6 μV in the area $U_G < 0.6$ V and more than an order of magnitude smaller than the maximal dc photovoltage of 56 μV at strong gate asymmetry, as seen in Fig. 3A. As a result, the discussed effects are unable to explain the observed photoresponse.

By using the detection principle based on the discovered phenomenon, a new class of photoelectric tunable-step (PETS) THz detectors can be developed. PETS detectors offer several remarkable properties when compared to state-of-the-art THz detection technologies. The photoresponse is observed under normal incidence of radiation. Compared to intersubband-based detectors such as QWIPs and TACITs, in PETS detectors, the electric field of the wave and the desired direction of the photoelectron momentum are perfectly aligned in the same direction by design, which eliminates the need for complex light-coupling architectures and offers easy fabrication. This also means that no scattering is required to redirect electrons, and because the photoexcitation is a quantum mechanical, instantaneous process, it follows that the mechanism does not have an intrinsic response time limit. In addition, compared to detectors based on the conventional, 3D photoelectric effect (HEIWIP and HIWIP), the potential step height V_B is in situ gate-voltage tunable, and the presented mechanism offers detection at zero source-drain bias. Schottky detectors, which operate at the low-frequency end of the THz range, provide sensitive room temperature detection but have a rapid falloff of the responsivity with frequency $\sim\omega^{-2}$ (*26*, *27*), resulting in a low output above ~1 THz. By contrast, the theoretically expected roll-off of the in-plane photoelectric effect is much weaker, $\sim\omega^{-1/2}$. Superconducting hot electron bolometers provide both high sensitivity and high bandwidth but have to be operated around half of the critical temperature of the superconducing material, around 8 K for the commonly used NbN material, and are therefore restricted to cryogenic temperatures (*29*–*31*). The experiment presented here was conducted at 9-K temperature; however, when the sample temperature is increased from 9 to 19 K, the photovoltage amplitude becomes only 2.3 times less. Because the in-plane photoelectric effect is a phenomenon observed within a degenerate Fermi gas, with $k_B T \ll \mu$, the mechanism is expected to be robust to temperature changes. Plasmonic detectors based on field-effect transistors provide sensitive room temperature detection across the range of 1 to 5 THz (*38*, *41*, *42*, *44*, *63*). Because the in-plane photoelectric effect yields a substantially higher response than other photoresponse-generating mechanisms previously considered in 2D electron systems, the realization of detection via this mechanism, potentially combined with plasmonic enhancement, offers a way of realizing more sensitive THz detectors that could provide an alternative to or replace state-of-the-art Schottky diodes or superconducting hot electron bolometers in applications requiring small size, low cost, and easy integration. High-electron-mobility wafer heterostructures similar to those used in this work are readily available commercially, and the PETS detector design offers easy optimization via modifications of the lithographic design without the need of redesigning and regrowing the wafer heterostructure for each iteration—features that will simplify and reduce cost of commercialization of such detectors. In addition, the dual-gated device architecture allows independent tuning of output impedance and responsivity of the detectors. This facilitates integration into external circuits and will advance the development of high-speed, large-scale THz focal plane arrays and communication systems, which will shape the future of THz technology.

Further experimental and theoretical research studies, including studies of the temperature and frequency dependencies of the in-plane photoelectric effect on the GaAs/AlGaAs and other semiconductor systems, are needed to improve the performance of PETS detectors. Another challenge is to maximize the transfer of THz power from the antenna to the electrons in the 2DEG in the vicinity of the potential step (i.e., impedance matching of the THz antenna), to improve the sensitivity.

In conclusion, we demonstrated a fundamental physical phenomenon that has not been observed or predicted previously—the in-plane photoelectric effect. It is a purely quantum-mechanical, scattering-free phenomenon. The maximum photocurrent is obtained when the chemical potential lies above the potential step in both parts of the 2DEG, i.e., the 2DEG is degenerate. Such a situation has not been implemented so far and would not work in the case of the conventional, 3D photoelectric effect. The effect is substantially stronger than THz photoresponse mechanisms previously considered in 2D electron systems. The potential step is artificially created and tunable by gate voltages, and no dc source-drain bias is required to observe the photoresponse. The theory shows that the effect is ideally suited for utilization across the whole THz range. As an inherent effect of 2D systems, it can be used in 2DEGs on the basis of III-V materials, silicon, and the novel 2D layered, graphene-related materials.

MATERIALS AND METHODS

Sample fabrication

The heterostructure used was deposited on a GaAs semi-insulating substrate. The sequence grown by molecular beam epitaxy was, after a 1-μm undoped GaAs buffer layer, 40-nm undoped $Al_{0.33}Ga_{0.67}As$; 40-nm n-doped $Al_{0.33}Ga_{0.67}As$ with $10^{18}/cm^3$ doping density of Si donors; and 10-nm GaAs cap. The wafer was characterized using an ungated Hall bar in a magnetic field. The 2DEG in the wafer has an electron density of $\sim 3.7 \cdot 10^{11}/cm^2$ and a mobility in excess of 1.1×10^6 $cm^2/(Vs)$ at 1.5 K, which corresponds to a scattering time of $\tau = 42$ ps and a mean free path of 11 μm. The antenna design was optimized using numerical finite-element simulations in COMSOL Multiphysics (see details in Supplementary Text and figs. S2 and S3). The simulations yield an absorption cross section of the antenna of $(22.5\ \mu m)^2$ at 1.9 THz. To process the sample, electron beam lithography was used to define an etch mask using ma-N 2410 resist onto the as-grown wafer. At this stage, the sample was etched wet chemically to form a 100-nm-high mesa with the narrow channel and areas for contact pads. The ohmic source and drain contacts to the channel were processed using optical lithography by annealing an AuGeNi eutectic alloy. Next, electron beam lithography with poly(methyl methacrylate) resist was used to define a TiAu gate structure on top of the device to create a bow-tie antenna that focuses the radiation onto the channel. Optical lithography was used for creation of large-area TiAu bond pads. Last, the sample was encapsulated in Shipley S1805 resist for surface protection.

Edge depletion

The lithographically defined channel width is 2.0 μm. Calibration of the mesa etching has shown that sideway etching of 165 nm occurs

Downloaded from https://www.science.org at Universitaetsbibliothek Augsburg on May 23, 2022

on average on either side of the mesa, so the actual mesa width is approximately 1.67 μm. Measurements on other samples created by this process have shown that the lateral edge depletion of the 2DEG is between 0.34 and 0.58 μm. Taking this into account, the actual width W of the 2DEG in the channel is between 0.5 and 1 μm and is assumed to be 0.7 μm in the theory.

Electrical measurement setup

The conductance in Fig. 3A was calculated as the ratio of current to voltage when the sample was driven with a 1.6-mV sine wave at 86.5 Hz. The current is passed through source 1 and drain 1, and the voltage is measured from source 2 to drain 2 in Fig. 2A.

Determination of the power density at the sample

To illuminate the sample with THz radiation, we constructed a setup coupling together two liquid-helium continuous-flow cryostats: one with a 1.9-THz single-plasmon bound-to-continuum THz QCL (i.e., the THz source) and the other with the sample, using a copper waveguide. The QCL design is the same as in (*57*) but with 4.4-nm instead of 5.0-nm injection barrier thickness. This waveguided setup allows quantitative determination of the THz intensity at the sample space. Before measurements, the QCL cryostat is first aligned so as to induce maximum photoresponse of the sample. After the measurements, the sample is warmed up and removed, while the QCL is kept lasing, and its temperature (18 K) and alignment are maintained. The total transmitted power at the sample space is then determined using a Thomas Keating absolute power meter, while the intensity distribution is measured using a Golay cell with a 1-mm aperture on a setup with motorized xy scanning stages. We thus find the time-averaged intensity $\langle I\rangle \approx 6.3\ \mu W/mm^2$ at the sample space at the mode profile peak, where the intensity distribution reaches its maximum value. This intensity value does not take into account interference effects. By observing the oscillations of the device's photoresponse when moving the z position of the QCL and hence tuning the path length between THz source and our antenna-coupled detector, we estimate that, under constructive interference, the intensity at the position of the THz antenna can be up to 74% higher than the average intensity value.

Photocurrent calculation

The dynamics of photoexcited electrons is determined by the time-dependent Schrödinger equation

$$i\hbar\frac{\partial\Psi}{\partial t} = -\frac{\hbar^2}{2m_{\mathrm{eff}}}\frac{\partial^2\Psi}{\partial x^2} - \frac{\hbar^2}{2m_{\mathrm{eff}}}\frac{\partial^2\Psi}{\partial y^2} + V_0(x)\Psi + V_1(x,t)\Psi \quad (3)$$

In the transverse, y direction, we assume infinite potential walls at $y = 0$ and $y = W$, which give quantization energies of $E_W n^2$, where $E_W = \pi^2\hbar^2/(2m_{\mathrm{eff}}W^2) \approx 12\ \mu eV$ and n is the subband index.

In zeroth order, i.e., without $V_1(x, t)$, we calculate the transmission coefficient of the potential step from the above equation. For a given particle energy E, it is

$$T^{(0)}_{E,n}(E) = \mathrm{T}_0(\mathcal{E}) = \Theta(\mathcal{E}-1)\frac{4\sqrt{\mathcal{E}(\mathcal{E}-1)}}{|\sqrt{\mathcal{E}}+\sqrt{\mathcal{E}-1}|^2};\ \text{with}\ \mathcal{E} = \frac{E - E_W n^2 - V_{\mathrm{R}}}{V_{\mathrm{B}}} \quad (4)$$

and does not depend on the direction of motion of the particle (whether it is incident from the left or from the right). Here, $V_{\mathrm{B}} = V_{\mathrm{L}} - V_{\mathrm{R}}$ is the height of the potential step. The above formula yields the conductance of the potential step when integrated over the electron energy states

$$\frac{\sigma}{e^2/\pi\hbar} = \frac{1}{4k_{\mathrm{B}}T}\sum_{n=1}^{\infty}\int_{-\infty}^{\infty}\frac{T^{(0)}_{E,n}(E)\,\mathrm{d}E}{\cosh^2\left(\frac{E-\mu}{2k_{\mathrm{B}}T}\right)} \quad (5)$$

Solving Eq. 3 with V_1 as perturbation, we calculate the wave functions in zero and first order, and from them, the particle flows $j^{0\leftarrow}_{E,n}$, $j^{0\rightarrow}_{E,n}$ and $j^{+\leftarrow}_{E,n}$, $j^{+\rightarrow}_{E,n}$. Here, $j^{0\leftarrow}_{E,n}$ is the flow of particles with energy E incident onto the step from the right, and $j^{+\leftarrow}_{E,n}$ is the flow of particles with energy $E + \hbar\omega$ having passed the step and moving to the left (the definitions for moving to the right, "→," are similar). Their ratio leads to the first-order transmission coefficients of particles having absorbed a THz quantum $\hbar\omega$, defined as $T^{+\rightarrow}_{E,n} = j^{+\rightarrow}_{E,n}/j^{0\rightarrow}_{E,n}$ for the positive and $T^{+\leftarrow}_{E,n} = j^{+\leftarrow}_{E,n}/j^{0\leftarrow}_{E,n}$ for the negative x direction of motion. The first-order reflection coefficients can be obtained in a similar way. The calculated transmission coefficients can be written in the form $T^{+\rightleftarrows}_{E,n} = \alpha P^{\rightleftarrows}(E - E_W n^2, \hbar\omega, V_{\mathrm{L}}, V_{\mathrm{R}})$, where $\alpha = (eE_{\mathrm{ac}}b/\hbar\omega)^2$ and the functions $P^{\rightleftarrows}(E, \hbar\omega, V_{\mathrm{L}}, V_{\mathrm{R}})$ are illustrated in Fig. 1C for $\hbar\omega = 8$ meV, $V_{\mathrm{L}} = 5$ meV, and $V_{\mathrm{R}} = -5$ meV. While the zero-order transmission coefficients do not depend on the direction of electron flow, this is not the case for the first-order transmission coefficients. For all energies, $T^{+\leftarrow}_{E,n} > T^{+\rightarrow}_{E,n}$, provided that $V_{\mathrm{L}} > V_{\mathrm{R}}$, which is also seen in the plot. This means that the particles flow onto the step. The photocurrent I_{ph} is then calculated as

$$I_{\mathrm{ph}} = -\frac{e}{\pi\hbar}\sum_{n=1}^{\infty}\int_{-\infty}^{\infty}\mathrm{d}E(T^{+\rightarrow}_{E,n} - T^{+\leftarrow}_{E,n})f(E,\mu,T)\,(1 - f(E+\hbar\omega,\mu,T)) \quad (6)$$

where the factors containing the Fermi distribution function $f(E, \mu, T)$ take into account the occupation of electron states and μ is the chemical potential of the unbiased system. Equation 1 is obtained from Eq. 6 at temperature $T = 0$.

The perturbation theory parameter α should be ≪1 for the applicability of the theory. With the incident intensity of I_0 during a THz pulse, the electric field in the x direction acting on the 2DEG between the gates is $E_{\mathrm{ac},\,x} \approx 100$ V/cm according to the numerical antenna simulations in COMSOL Multiphysics. This gives $eE_{\mathrm{ac}}b \approx 2.7$ meV and $\alpha \approx 0.12 \ll 1$, which justifies the perturbative approach and neglection of higher-order contributions to the photocurrent.

SUPPLEMENTARY MATERIALS

Supplementary material for this article is available at https://science.org/doi/10.1126/sciadv.abi8398

REFERENCES AND NOTES

1. P. Lenard, Über die lichtelektrische Wirkung. *Ann. Phys.* **313**, 149–198 (1902).
2. A. Einstein, Über einen die Erzeugung und Verwandlung des Lichtes betreffenden heuristischen Gesichtspunkt. *Ann. Phys.* **322**, 132–148 (1905).
3. K. K. Choi, *The Physics of Quantum Well Infrared Photodetectors* (World Scientific Publishing Co. Pte. Ltd., 1997).
4. J. Andersson, L. Lundqvist, Z. Paska, Quantum efficiency enhancement of AlGaAs/GaAs quantum well infrared detectors using a waveguide with a grating coupler. *Appl. Phys. Lett.* **58**, 2264–2266 (1991).
5. P. Martyniuk, A. Rogalski, Quantum-dot infrared photodetectors: Status and outlook. *Progr. Quantum Electron.* **32**, 89–120 (2008).
6. E. Haller, M. Hueschen, P. Richards, Ge:Ga photoconductors in low infrared backgrounds. *Appl. Phys. Lett.* **34**, 495–497 (1979).
7. G. Stacey, J. Beeman, E. Haller, N. Geis, A. Poglitsch, M. Rumitz, Stressed and unstressed Ge:Ga detector arrays for airborne astronomy. *Int. J. Infrared Millimeter Waves* **13**, 1689–1707 (1992).

Downloaded from https://www.science.org at Universitaetsbibliothek Augsburg on May 23, 2022

8. A. Perera, R. Sherriff, M. Francombe, R. Devaty, Far infrared photoelectric thresholds of extrinsic semiconductor photocathodes. *Appl. Phys. Lett.* **60**, 3168–3170 (1992).
9. A. Perera, H. Yuan, M. Francombe, Homojunction internal photoemission far-infrared detectors: Photoresponse performance analysis. *J. Appl. Phys.* **77**, 915–924 (1995).
10. W. Shen, Recent progress in mid-and far-infrared semiconductor detectors. *Int. J. Infrared Millimeter Waves* **21**, 1739–1746 (2000).
11. Y. F. Lao, A. G. U. Perera, L. H. Li, S. P. Khanna, E. H. Linfield, H. C. Liu, Tunable hot-carrier photodetection beyond the bandgap spectral limit. *Nat. Photonics* **8**, 412–418 (2014).
12. M. S. Sherwin, Tunable antenna-coupled intersubband terahertz (TACIT) detector, U.S. Patent 5914497A (1997).
13. C. Cates, G. Briceno, M. Sherwin, K. Maranowski, K. Campman, A. Gossard, A concept for a tunable antenna-coupled intersubband terahertz (TACIT) detector. *Physica E* **2**, 463–467 (1998).
14. C. Yoo, M. Huang, J. Kawamura, K. West, L. Pfeiffer, B. Karasik, M. Sherwin, Demonstration of a tunable antenna-coupled intersubband terahertz (TACIT) mixer. *Appl. Phys. Lett.* **116**, 013504 (2020).
15. S. D. Gunapala, D. R. Rhiger, C. Jagadish, *Advances in Infrared Photodetectors* (Elsevier, 2011).
16. A. G. U. Perera, G. Ariyawansa, P. V. V. Jayaweera, S. G. Matsik, M. Buchanan, H. C. Liu, Semiconductor terahertz detectors and absorption enhancement using plasmons. *Microelectronics J.* **39**, 601–606 (2008).
17. W. Z. Shen, A. Perera, H.-C. Liu, M. Buchanan, W. Schaff, Bias effects in high performance GaAs homojunction far-infrared detectors. *Appl. Phys. Lett.* **71**, 2677–2679 (1997).
18. P. Bai, Y. Zhang, X. Guo, Z. Fu, J. Cao, W. Shen, Realization of the high-performance THz GaAs homojunction detector below the frequency of Reststrahlen band. *Appl. Phys. Lett.* **113**, 241102 (2018).
19. H. Ghimire, P. Jayaweera, D. Somvanshi, Y. Lao, A. Perera, Recent progress on extended wavelength and split-off band heterostructure infrared detectors. *Micromachines* **11**, 547 (2020).
20. J. K. Sass, Evidence for an anisotropic volume photoelectric effect in polycrystalline nearly free electron metals. *Surf. Sci.* **51**, 199–212 (1975).
21. I. Tamm, S. Schubin, Zur Theorie des Photoeffektes an Metallen. *Z. Phys.* **68**, 97–113 (1931).
22. K. Mitchell, The theory of the surface photoelectric effect in metals—I. *Proc. R. Soc. Lond. A* **146**, 442–464 (1934).
23. J. Girardeau-Montaut, C. Girardeau-Montaut, S. Moustaizis, C. Fotakis, Dependence of femtosecond single-photon photoemission from gold on laser beam incidence and polarization. *Appl. Phys. Lett.* **63**, 699–701 (1993).
24. C. N. Berglund, W. E. Spicer, Photoemission studies of copper and silver: Theory. *Phys. Rev.* **136**, A1030–A1044 (1964).
25. Data from Virginia Diodes Inc., Charlottesville, USA.
26. M. McColl, D. Hoidges, W. Garber, Submillimeter-wave detection with submicron-size Schottky-barrier diodes. *IEEE Trans. Microw. Theory Tech.* **25**, 463–467 (1977).
27. F. Sizov, A. Rogalski, THz detectors. *Prog. Quantum Electron.* **34**, 278–347 (2010).
28. S. Matsik, M. Rinzan, A. Perera, H. Liu, Z. Wasilewski, M. Buchanan, Cutoff tailorability of heterojunction terahertz detectors. *Appl. Phys. Lett.* **82**, 139–141 (2003).
29. M. Hajenius, J. Baselmans, J. Gao, T. Klapwijk, P. De Korte, B. Voronov, G. Gol'tsman, Low noise NbN superconducting hot electron bolometer mixers at 1.9 and 2.5 THz. *Supercond. Sci. Technol.* **17**, S224–S228 (2004).
30. A. Shurakov, Y. Lobanov, G. Goltsman, Superconducting hot-electron bolometer: From the discovery of hot-electron phenomena to practical applications. *Supercond. Sci. Technol.* **29**, 023001 (2016).
31. A. Rogalski, *Infrared and Terahertz Detectors* (CRC Press, 2019).
32. J. Q. Lü, M. S. Shur, J. L. Hesler, L. Sun, R. Weikle, Terahertz detector utilizing two-dimensional electronic fluid. *IEEE Electron Device Lett.* **19**, 373–375 (1998).
33. W. Knap, V. Kachorovskii, Y. Deng, S. Rumyantsev, J.-Q. Lü, R. Gaska, M. S. Shur, G. Simin, X. Hu, M. A. Khan, C. A. Saylor, L. C. Brunel, Nonresonant detection of terahertz radiation in field effect transistors. *J. Appl. Phys.* **91**, 9346–9353 (2002).
34. W. Knap, S. Nadar, H. Videlier, S. Boubanga-Tombet, D. Coquillat, N. Dyakonova, F. Teppe, K. Karpierz, J. Łusakowski, M. Sakowicz, I. Kasalynas, D. Seliuta, G. Valusis, T. Otsuji, Y. Meziani, A. El Fatimy, S. Vandenbrouk, K. Madjour, D. Théron, C. Gaquière, Field effect transistors for terahertz detection and emission. *J. Infrared Millim. Terahertz Waves* **32**, 618–628 (2011).
35. R. Al Hadi, H. Sherry, J. Grzyb, Y. Zhao, W. Forster, H. M. Keller, A. Cathelin, A. Kaiser, U. R. Pfeiffer, A 1 k-pixel video camera for 0.7–1.1 terahertz imaging applications in 65-nm CMOS. *IEEE J. Solid-State Circuits* **47**, 2999–3012 (2012).
36. J. Sun, Y. Sun, D. Wu, Y. Cai, H. Qin, B. Zhang, High-responsivity, low-noise, room-temperature, self-mixing terahertz detector realized using floating antennas on a GaN-based field-effect transistor. *Appl. Phys. Lett.* **100**, 013506 (2012).
37. T. Otsuji, Trends in the research of modern terahertz detectors: Plasmon detectors. *IEEE Trans. Terahertz Sci. Technol.* **5**, 1110–1120 (2015).
38. S. Regensburger, A. K. Mukherjee, S. Schönhuber, M. A. Kainz, S. Winnerl, J. M. Klopf, H. Lu, A. C. Gossard, K. Unterrainer, S. Preu, Broadband terahertz detection with zero-bias field-effect transistors between 100 GHz and 11.8 THz with a noise equivalent power of 250 pW/$\sqrt{\text{Hz}}$ at 0.6 THz. *IEEE Trans. Terahertz Sci. Technol.* **8**, 465–471 (2018).
39. A. Zak, M. A. Andersson, M. Bauer, J. Matukas, A. Lisauskas, H. G. Roskos, J. Stake, Antenna-integrated 0.6 THz FET direct detectors based on CVD graphene. *Nano Lett.* **14**, 5834–5838 (2014).
40. L. Viti, J. Hu, D. Coquillat, A. Politano, C. Consejo, W. Knap, M. S. Vitiello, Heterostructured hBN-BP-hBN Nanodetectors at Terahertz Frequencies. *Adv. Mater.* **28**, 7390–7396 (2016).
41. S. Boppel, A. Lisauskas, M. Mundt, D. Seliuta, L. Minkevicius, I. Kasalynas, G. Valusis, M. Mittendorff, S. Winnerl, V. Krozer, H. G. Roskos, CMOS integrated antenna-coupled field-effect transistors for the detection of radiation from 0.2 to 4.3 THz. *IEEE Trans. Microw. Theory Techn.* **60**, 3834–3843 (2012).
42. M. Bauer, R. Venckevičius, I. Kašalynas, S. Boppel, M. Mundt, L. Minkevičius, A. Lisauskas, G. Valušis, V. Krozer, H. Roskos, Antenna-coupled field-effect transistors for multi-spectral terahertz imaging up to 4.25 THz. *Opt. Express* **22**, 19235–19241 (2014).
43. K. Ikamas, A. Lisauskas, S. Boppel, Q. Hu, H. G. Roskos, Efficient detection of 3 THz radiation from quantum cascade laser using silicon CMOS detectors. *J. Infrared Millim. Terahertz Waves* **38**, 1183–1188 (2017).
44. S. Preu, M. Mittendorff, S. Winnerl, H. Lu, A. Gossard, H. B. Weber, Ultra-fast transistor-based detectors for precise timing of near infrared and THz signals. *Opt. Express* **21**, 17941–17950 (2013).
45. M. Dyakonov, M. Shur, Detection, mixing, and frequency multiplication of terahertz radiation by two-dimensional electronic fluid. *IEEE Trans. Electron Devices* **43**, 380–387 (1996).
46. A. Lisauskas, U. Pfeiffer, E. Öjefors, P. H. Bolìvar, D. Glaab, H. G. Roskos, Rational design of high-responsivity detectors of terahertz radiation based on distributed self-mixing in silicon field-effect transistors. *J. Appl. Phys.* **105**, 114511 (2009).
47. L. Molenkamp, H. Van Houten, C. Beenakker, R. Eppenga, C. Foxon, Quantum oscillations in the transverse voltage of a channel in the nonlinear transport regime. *Phys. Rev. Lett.* **65**, 1052–1055 (1990).
48. N. M. Gabor, J. C. Song, Q. Ma, N. L. Nair, T. Taychatanapat, K. Watanabe, T. Taniguchi, L. S. Levitov, P. Jarillo-Herrero, Hot carrier–assisted intrinsic photoresponse in graphene. *Science* **334**, 648–652 (2011).
49. L. Viti, A. R. Cadore, X. Yang, A. Vorobiev, J. E. Muench, K. Watanabe, T. Taniguchi, J. Stake, A. C. Ferrari, M. S. Vitiello, Thermoelectric graphene photodetectors with sub-nanosecond response times at terahertz frequencies. *Nanophotonics* **10**, 89–98 (2021).
50. J. Song, G. Aizin, J. Mikalopas, Y. Kawano, K. Ishibashi, N. Aoki, J. Reno, Y. Ochiai, J. Bird, Bolometric terahertz detection in pinched-off quantum point contacts. *Appl. Phys. Lett.* **97**, 083109 (2010).
51. A. D. Levin, G. M. Gusev, Z. D. Kvon, A. K. Bakarov, N. A. Savostianova, S. A. Mikhailov, E. E. Rodyakina, A. V. Latyshev, Giant microwave photo-conductance of a tunnel point contact with a bridged gate. *Appl. Phys. Lett.* **107**, 072112 (2015).
52. L. Kouwenhoven, S. Jauhar, K. McCormick, D. Dixon, P. McEuen, Y. V. Nazarov, N. Van Der Vaart, C. Foxon, Photon-assisted tunneling through a quantum dot. *Phys. Rev. B* **50**, 2019–2022 (1994).
53. S. Verghese, R. Wyss, T. Schäpers, A. Förster, M. Rooks, Q. Hu, Photon-assisted transport through quantized energy states in a lateral dual-gate device. *Phys. Rev. B* **52**, 14834–14838 (1995).
54. O. A. Tkachenko, V. A. Tkachenko, Z. D. Kvon, Photon-assisted electron transport through a quantum point contact in a microwave field. *JETP Lett.* **102**, 378–382 (2015).
55. M. Otteneder, Z. Kvon, O. Tkachenko, V. Tkachenko, A. Jaroshevich, E. Rodyakina, A. Latyshev, S. Ganichev, Giant terahertz photoconductance of quantum point contacts in the tunneling regime. *Phys. Rev. Appl* **10**, 014015 (2018).
56. R. Degl'Innocenti, L. Xiao, D. S. Jessop, S. J. Kindness, Y. Ren, H. Lin, J. A. Zeitler, J. A. Alexander-Webber, H. J. Joyce, P. Braeuninger-Weimer, S. Hofmann, H. E. Beere, D. A. Ritchie, Fast room-temperature detection of terahertz quantum cascade lasers with graphene-loaded bow-tie plasmonic antenna arrays. *ACS Photonics* **3**, 1747–1753 (2016).
57. C. Worrall, J. Alton, M. Houghton, S. Barbieri, H. E. Beere, D. Ritchie, C. Sirtori, Continuous wave operation of a superlattice quantum cascade laser emitting at 2 THz. *Opt. Express* **14**, 171–181 (2006).
58. J. Blakemore, Semiconducting and other major properties of gallium arsenide. *J. Appl. Phys.* **53**, R123–R181 (1982).
59. Y. Hirayama, K. Muraki, T. Saku, Two-dimensional electron gas formed in a back-gated undoped heterostructure. *Appl. Phys. Lett.* **72**, 1745–1747 (1998).
60. V. Mokerov, Y. V. Fedorov, A. Hook, High density 2DEG in III-V semiconductor heterostructures and high-electron-mobility transistors based on them. *Semiconductors* **33**, 970–971 (1999).
61. T. Janssen, J. Maan, J. Singleton, N. Patel, M. Pepper, J. Frost, D. Ritchie, G. Jones, A new mechanism for high-frequency rectification in a ballistic quantum point contact. *J. Phys. Condens. Matter* **6**, L163 (1994).

Downloaded from https://www.science.org at Universitaetsbibliothek Augsburg on May 23, 2022

62. S. Nadar, H. Videlier, D. Coquillat, F. Teppe, M. Sakowicz, N. Dyakonova, W. Knap, D. Seliuta, I. Kašalynas, G. Valušis, Room temperature imaging at 1.63 and 2.54 THz with field effect transistor detectors. *J. Appl. Phys.* **108**, 054508 (2010).
63. J. Zdanevičius, D. Čibiraitė, K. Ikamas, M. Bauer, J. Matukas, A. Lisauskas, H. Richter, T. Hagelschuer, V. Krozer, H.-W. Hübers, Field-effect transistor based detectors for power monitoring of THz quantum cascade lasers. *IEEE Trans. Terahertz Sci. Technol.* **8**, H. G. Roskos, 613–H. G. Ros621 (2018).
64. R. L. Olmon, B. Slovick, T. W. Johnson, D. Shelton, S.-H. Oh, G. D. Boreman, M. B. Raschke, Optical dielectric function of gold. *Phys. Rev. B* **86**, 235147 (2012).
65. W. Michailow, P. Spencer, N. W. Almond, S. J. Kindness, R. Wallis, T. A. Mitchell, R. Degl'Innocenti, S. A. Mikhailov, H. E. Beere, D. A. Ritchie, Research data supporting "An in-plane photoelectric effect in two-dimensional electron systems for terahertz detection". Apollo - University of Cambridge Repository (2022).

Acknowledgments
We thank Binbin Wei, Yuqing Wu, Ateeq Nasir, Chong Chen, Ben Ramsay, and Antonio Rubino for helpful advice, as well as Abbie Lowe and Jonathan Griffiths for help with electron beam lithography. We express special thanks to Joanna Waldie for advice on sample fabrication and measurements and comments on the manuscript. **Funding:** W.M. thanks the George and Lillian Schiff Studentship of the University of Cambridge for financial support and is grateful for the Honorary Vice-Chancellor's Award of the Cambridge Trust. S.A.M. acknowledges funding from the European Union's Horizon 2020 research and innovation program Graphene Core 3 under grant agreement no. 881603. R.D. acknowledges support from the EPSRC (grant no. EP/S019383/1). We acknowledge EPSRC funding under the HyperTerahertz grant (no. EP/P021859/1). **Author contributions:** W.M. conceived the device concept; designed, simulated, fabricated, and measured the samples; built the waveguide-coupled THz setup; and wrote the paper. P.S. advised on instrumental techniques and helped and supported in the laboratory. N.W.A. built the motorized Golay cell scanning setup. S.J.K. advised on COMSOL numerical simulations. R.W. advised on THz measurement techniques. T.A.M. did the lithographic electron beam exposure. R.D. participated in discussions of experimental findings. S.A.M. provided quantitative theory and corresponding contribution to the paper. H.E.B. grew the wafer material by molecular beam epitaxy and advised. D.A.R. enabled and supervised the research and advised. All authors discussed the results and the manuscript. **Competing interests:** The authors declare that they have no competing interests. **Data and materials availability:** All data needed to evaluate the conclusions in the paper are present in the paper and/or the Supplementary Materials. The data that support the findings of this study will be available in the Apollo repository of the University of Cambridge at https://doi.org/10.17863/CAM.58046 (*65*).

Submitted 7 April 2021
Accepted 26 February 2022
Published 15 April 2022
10.1126/sciadv.abi8398

Downloaded from https://www.science.org at Universitaetsbibliothek Augsburg on May 23, 2022

ScienceAdvances

An in-plane photoelectric effect in two-dimensional electron systems for terahertz detection

Wladislaw MichailowPeter SpencerNikita W. AlmondStephen J. KindnessRobert WallisThomas A. MitchellRiccardo Degl'InnocentiSergey A. MikhailovHarvey E. BeereDavid A. Ritchie

Sci. Adv., 8 (15), eabi8398. • DOI: 10.1126/sciadv.abi8398

View the article online
https://www.science.org/doi/10.1126/sciadv.abi8398
Permissions
https://www.science.org/help/reprints-and-permissions

Downloaded from https://www.science.org at Universitaetsbibliothek Augsburg on May 23, 2022

Use of this article is subject to the Terms of service

Science Advances (ISSN) is published by the American Association for the Advancement of Science. 1200 New York Avenue NW, Washington, DC 20005. The title *Science Advances* is a registered trademark of AAAS.
Copyright © 2022 The Authors, some rights reserved; exclusive licensee American Association for the Advancement of Science. No claim to original U.S. Government Works. Distributed under a Creative Commons Attribution License 4.0 (CC BY).